

[advances.sciencemag.org/cgi/content/full/7/29/eabe5257/DC1](https://advances.sciencemag.org/cgi/content/full/7/29/eabe5257/DC1)

## Supplementary Materials for

### **Fully 3D-printed soft robots with integrated fluidic circuitry**

Joshua D. Hubbard, Ruben Acevedo, Kristen M. Edwards, Abdullah T. Alsharhan, Ziteng Wen, Jennifer Landry,  
Kejin Wang, Saul Schaffer, Ryan D. Sochol\*

\*Corresponding author. Email: rsochol@umd.edu

Published 14 July 2021, *Sci. Adv.* 7, eabe5257 (2021)  
DOI: 10.1126/sciadv.abe5257

#### **The PDF file includes:**

Supplementary Text  
Figs. S1 to S7  
Legends for movies S1 to S7

#### **Other Supplementary Material for this manuscript includes the following:**

(available at [advances.sciencemag.org/cgi/content/full/7/29/eabe5257/DC1](https://advances.sciencemag.org/cgi/content/full/7/29/eabe5257/DC1))

Movies S1 to S7

## **Supplementary Text**

### Soft Robotic “Finger” Finite Element Analysis (FEA) Simulations

Theoretical simulations of the bioinspired soft robotic “finger” (**Fig. S2A–C; Movie S4**) were performed using the commercial finite element analysis (FEA) software, COMSOL Multiphysics v.5.3a (COMSOL Inc., Sweden). Initially, the complete 3D CAD model (*i.e.*, including both materials fully assembled) was imported into the FEA software, and then the distinct material properties were set for the compliant and rigid components. Specifically, the compliant components were modeled as Agilus30 ( $E = 0.09 \text{ GPa}$ ;  $\rho = 1.125 \times 10^3 \text{ kg/m}^3$ ;  $\nu = 0.4$ ) while the rigid components were modeled as MED610 ( $E = 2.6 \text{ GPa}$ ;  $\rho = 1.175 \times 10^3 \text{ kg/m}^3$ ;  $\nu = 0.7$ ). Simulations were performed using the COSMOL Multiphysics “Solid Mechanics” module. The source pressure ( $P_s$ ) associated with inflation of the compliant bellowed components (*i.e.*, “knuckles”) was modeled as a boundary load on the internal surfaces. All other surfaces were set as free boundaries, with one end of the soft actuator assigned with a fixed constraint. The internal pressure corresponding to the  $P_s$  input was increased from 0 kPa to 150 kPa using increments of 10 kPa. All simulations were computed using the stationary (time-independent) solver and a parametric sweep function for applied loads.

### Experimental Characterization of Soft Robotic “Fingers” with Integrated Fluidic Transistors

Experiments with the integrated soft robotic finger-fluidic transistor systems were designed to elucidate soft actuator deformation behaviors—in particular, the vertical displacement of the fingertip—as a function of the  $P_s$  input after a fluidic transistor enters the closed state (*e.g.*,  $P_{G,High}$ ). For the pneumatic experiments to quantify deformation (**Fig. S2D–G; Movie S4**), a soft robotic finger-fluidic transistor system was connected to the Fluigent MFCS unit with one input connected to the source port (for regulating  $P_s$ ) while all other ports (*i.e.*, the drain ports, gate ports, and fingertip port) were sealed using luer caps (EW-30800-12, Cole-Parmer). Investigations of deformation characteristics were performed with an integrated soft robotic finger-fluidic transistor system by varying the magnitude of  $P_s$  (while all of the drain and gate ports were sealed). Specifically, a custom-designed script was generated in Fluigent Scite software and then run using the Fluigent MAESFLO software to increase the  $P_s$  input from 0 kPa to 50 kPa using stepped increments of 2 kPa every 10 s. One caveat, however, is that the compliant material used for the knuckles (Agilus30) is markedly flexible, such that even in the absence of a  $P_s$  input, the soft robotic finger exhibited a non-trivial degree of flaccid deformation (**Fig. S3D; Movie S4**). Thus, such initial displacements were set as a baseline from which to measure subsequent  $P_s$ -based deformations of the soft robotic finger. To quantify the displacement dynamics from video recorded using an EOS Rebel 1 camera (Canon, Tokyo, Japan), the digital image correlation (DIC) software, VIC-2D (Correlated Solutions, Irmo, SC), we employed for tracking and analysis (**Fig. S2D–G; Movie S4**). Subset and step sizes of 41 and 10, respectively, were used for the analysis along with a zero-normalized squared differences criterion. The full soft robotic finger was selected as the region of interest for tracking of the vertical displacements and the corresponding results were processed, quantified, and plotted using MATLAB 9.6 (MathWorks) (**Fig. S3G**).

### Support Removal Protocols for Modular Fluidic Circuit Elements

One key benefit of the smaller sizes of PolyJet-printed modular fluidic circuit elements (**Fig. S4**) is the ability to employ a primarily passive sacrificial support material removal process.

Specifically, the external as well as internally located sacrificial support material can be passively dissolved by submerging the printed components in a bath of 2% NaOH and 2% Na<sub>2</sub>SiO<sub>3</sub> (*w/w*) in DI water between six hours and one day (based on visual inspection) with continuous magnetic stirring and the solution exchanged every four to six hours (*e.g.*, **Fig. S5**). Lastly, all of the parts were removed from the solution bath and rinsed with DI water (in both internal and external regions).

### Fluidic Capacitor

We designed a PolyJet-based fluidic capacitor architecture that comprises distinct materials designed to complement component functionality, including: (*i*) a rigid material for the outer casing and internal channels, and (*ii*) a compliant material for the two inflating diaphragms (**Fig. S6A**). Under an applied pressure, the diaphragms deform outward (with respect to the magnitude of the pressure input), increasing the internal volume to store fluid (*e.g.*, liquid or air) (**Fig. S6B**). When the pressure input is terminated, however, the flexible diaphragms return to their initial states (**Fig. S6C**).

To investigate the potential for the boundary interface between the rigid and compliant materials to influence device integrity, we designed and printed six distinct interface geometries (**Fig. S6D–I**) and quantified interface performance through burst-pressure experimentation (**Fig. S6J**). Burst-pressure tests were performed by connecting one port to the Fluigent MFCS unit while sealing the opposing port with a luer cap (EW-30800-12, Cole-Parmer), and then increasing the input pressure using stepped increments of 2.5 kPa every 10 s until device rupture. Experimental results revealed that the two designs with straight interface geometries (**Fig. S6D**, **S6E**) outperformed their more complex counterparts (**Fig. S6I**). Because the differences in performance between the two designs was not statistically discernable ( $p = 0.90$ ), however, the double straight interface (**Fig. S6D**) was implemented not only for the fluidic capacitor, but for all rigid-compliant material interfaces in this work (*e.g.*, **Fig. 2**).

To provide insight into the relationship between the input pressure and the deformation of the flexible diaphragms, we connected one port of the fluidic capacitor to the Fluigent MFCS unit while sealing the opposing port with a luer cap (EW-30800-12, Cole-Parmer), and then inputted DI water under an applied pressure increasing from 0 kPa up to 100 kPa using stepped increments of 2.5 kPa every 10 s. We monitored the vertical displacement of each diaphragm during the experiments and then processed, quantified, and plotted the results using MATLAB 9.6 (MathWorks). The experimental results revealed a quasi-linear relationship for the pressure-displacement curve within the pressure range tested (**Fig. S6Q**), with displacement increasing up to  $6.2 \pm 0.4$  mm in response to an input pressure of 100 kPa (**Fig. S6P**).

### Alternative “Normally Open” Fluidic Transistor (Without $\gamma$ Architecture)

We also present an alternative fluidic transistor architecture that is similar to that of the  $\gamma_1$  “normally open” fluidic transistor, but with two key differences: (*i*) the intervening piston is removed; and (*ii*) the source-to-drain region diaphragm and gate region diaphragm are unified into a single diaphragm (**Fig. S7A**). Material rigidity-associated design features critical to element functionality, such as the compliant-material O-ring atop the central rigid-material piston as well as the rigid channels and outer structural casing, remain unchanged. Consequently, the operating principle is identical, with  $Q_{SD}$  unobstructed in the absence of a  $P_G$  input (**Fig. S7B**), but blocked upon the application of a  $P_G$  input of sufficient magnitude (**Fig. S7C**). The caveat to this architecture is that, because the diaphragms are no longer physically separated, the

pressure balance that dictates deformation is directly related such that the geometric means of modifying  $\gamma$  properties are not possible.

The experimental setup for characterization of the alternative fluidic transistor was identical to that of the  $\gamma$ -based “normally open” fluidic transistors, with: (i) the source input port connected to the Fluigent MFCS unit to regulate  $P_s$  of the input fluid (DI water); (ii) one of the drain output ports connected to a Fluigent Flow Unit flow rate sensor (Model L) to measure source-to-drain fluid flow ( $Q_{SD}$ ); (iii) one of the gate input ports connected to the Fluigent MFCS unit to regulate  $P_G$  of pressurized air; and (iv) the remaining two ports (one connected to the drain and once connected to the gate) sealed using luer caps (EW-30800-12, Cole-Parmer). One difference was that the custom-designed script—generated in Fluigent Scite software and then run using the Fluigent MAESFLO software—was designed to instead sweep through a linear range of  $P_s$  inputs corresponding to distinct, constant magnitudes of  $P_G$ . Specifically, the  $P_s$  input was increased from 0 kPa to 75 kPa using stepped increments of 2.5 kPa every 5 s for each constant  $P_G$  input, which ranged from 10 kPa to 50 kPa by increments of 10 kPa. All experiments were conducted under room temperature environment (20–25 °C). The magnitudes of  $Q_{SD}$ ,  $P_s$ , and  $P_G$  were recorded by the Fluigent software every 0.1 s throughout each experimental run. These results were processed, quantified, and plotted using MATLAB 9.6 (MathWorks, Natick, MA).

Quantified experimental results revealed distinct  $Q_{SD}$  behavior based on the interplay between the  $P_s$  and  $P_G$  inputs, with increases in the magnitude of the  $P_G$  input coinciding with a delay in the  $P_s$  associated with an onset in  $Q_{SD}$  (**Fig. S7D**). For the lowest  $P_G$  input tested (*i.e.*,  $P_G = 10$  kPa),  $Q_{SD}$  increased dramatically with increasing  $P_s$ , suggesting that the  $P_G$  input was not sufficient to initiate the sealed state. For the next largest  $P_G$  (*i.e.*,  $P_G = 20$  kPa), however,  $Q_{SD}$  appeared to be restricted up to  $P_s = 10.1 \pm 1.2$  kPa, above which  $Q_{SD}$  increased with a profile similar to that of the prior case. This trend continued for each of the  $P_G$  inputs examined, such as with the highest  $P_G$  case (*i.e.*,  $P_G = 50$  kPa) exhibiting  $Q_{SD}$  onset at  $P_s = 47.5 \pm 1.5$  kPa (**Fig. S7D**). These results suggest that this fluidic transistor architecture provides an effective means for gate regulation of  $Q_{SD}$ —with less material and a smaller height, and thus, faster print times compared to their  $\gamma$ -based counterparts—thereby offering utility for cases in which  $\gamma$  functionalities are not desired or required.

## Supplementary Figures

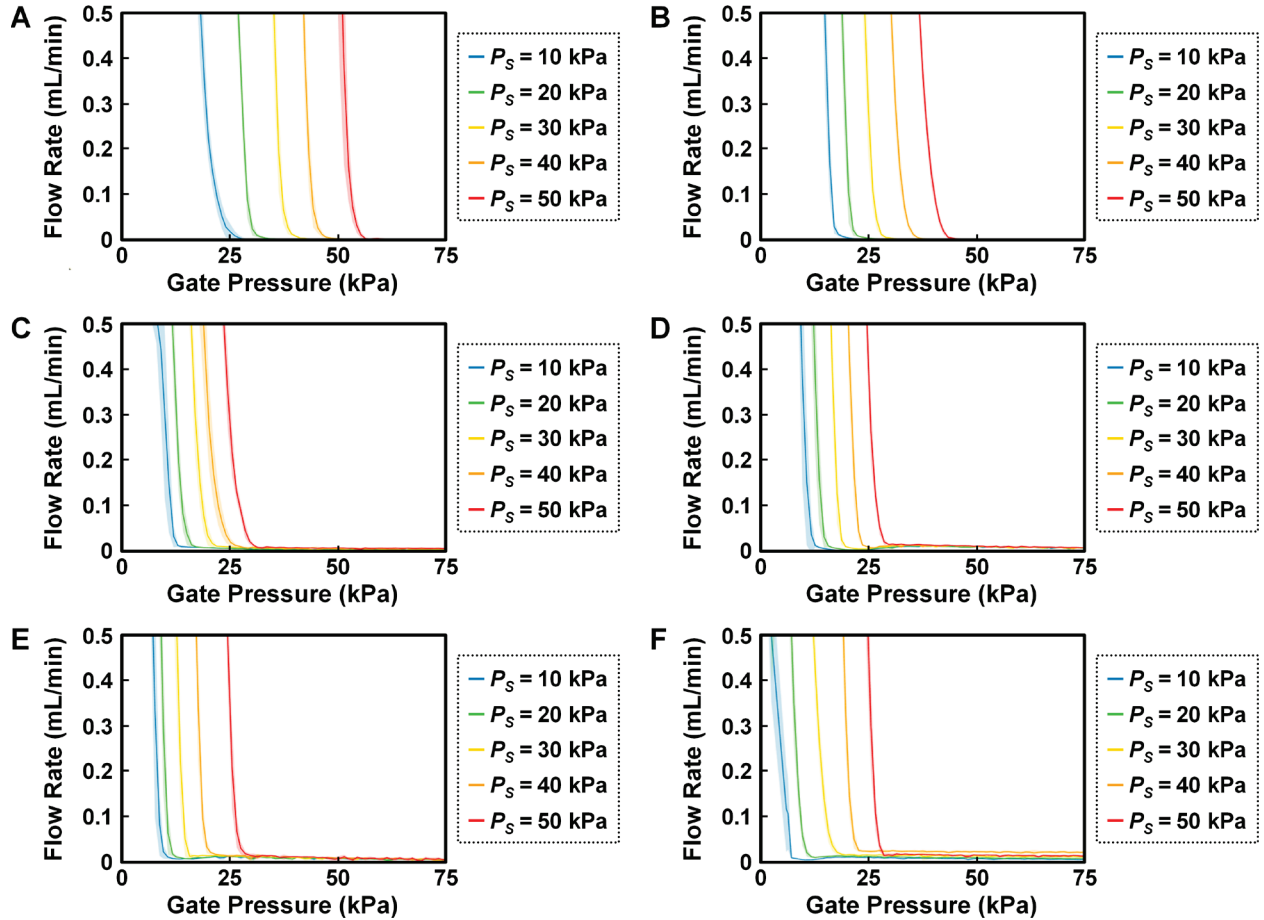


**Fig. S1.**

Quantified experimental results for source-to-drain fluid flow ( $Q_{SD}$ ) versus gate pressure ( $P_G$ ) corresponding to distinct, constant source pressure ( $P_S$ ) inputs for “normally closed” fluidic transistors designed with diaphragm area ratios of: (A) 1, (B) 1.5, (C) 2, (D) 2.5, (E) 3, and (F) 3.5. Error bands denote S.D.

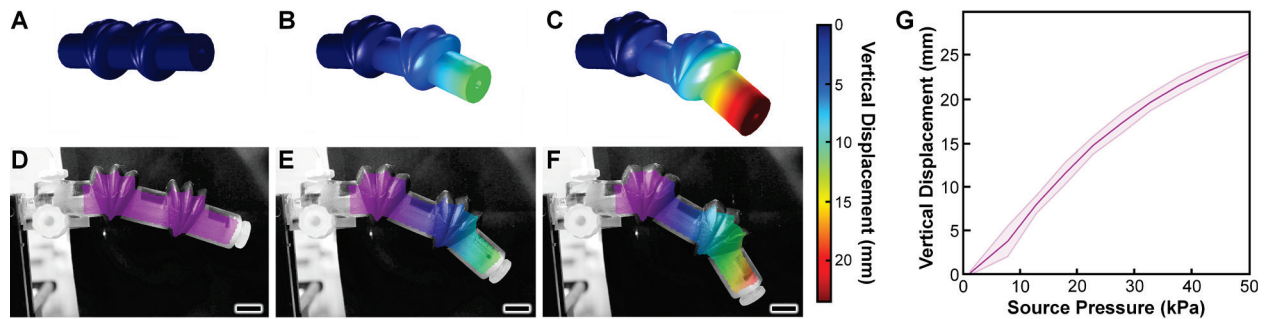


**Fig. S2.**

Theoretical and experimental results of deformation behaviour of the multi-material 3D soft robotic finger. (A–C) Theoretical COMSOL Multiphysics simulation results for deformation corresponding to input pressures of: (A) 0 kPa, (B) 10 kPa, and (C) 20 kPa. *See also Movie S3.* (D–F) Sequential digital image correlation (DIC)-processed images of an integrated soft robotic finger-fluidic transistor system corresponding to  $P_S$  inputs of: (D) 0 kPa, (E) 25 kPa, and (F) 50 kPa. Scale bars = 2 cm; *See also Movie S3.* (G) Quantified results for vertical displacement of the soft robotic fingertip as a function of  $P_S$ . Error bands denote *S.D.*

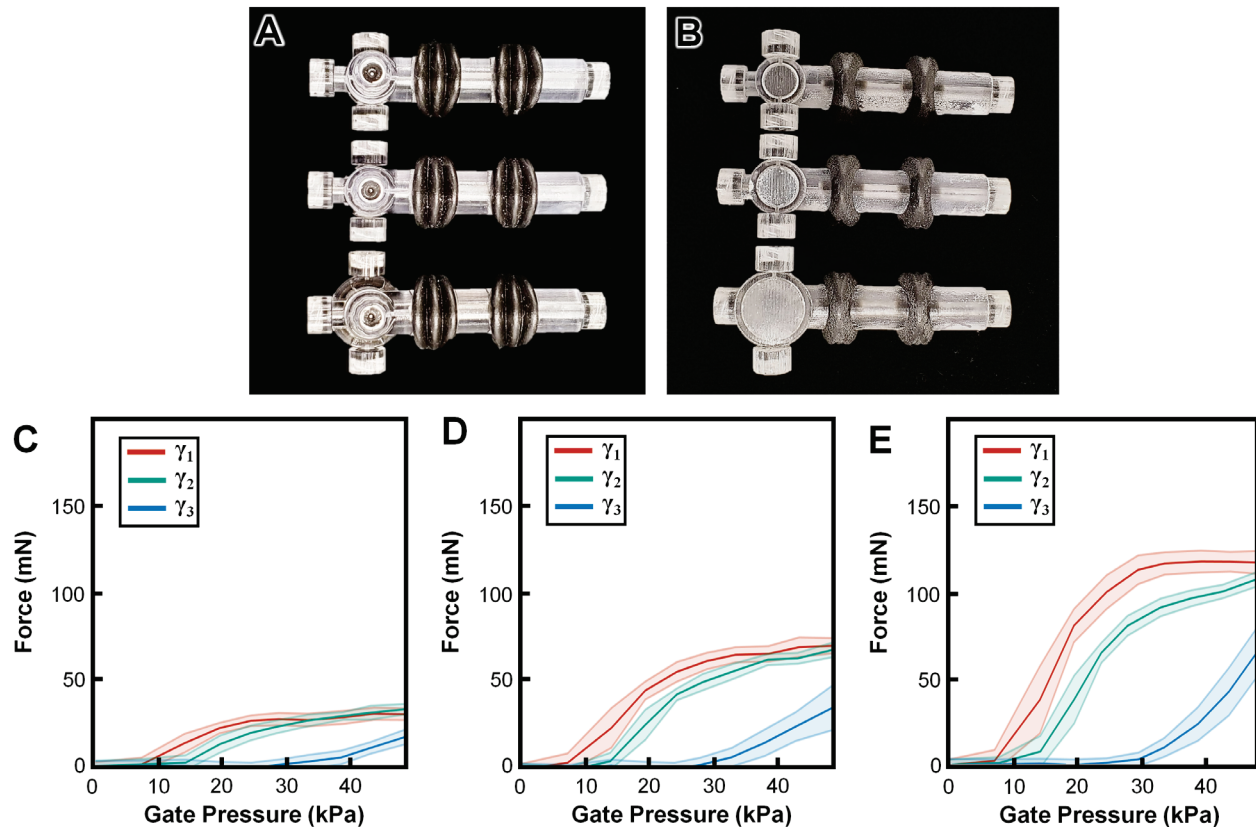


**Fig. S3.**

Results for multi-material 3D soft robotic fingers integrated with fluidic transistors with varying  $\gamma$  properties. (A, B) Fabrication results. (A) Top view and (B) bottom view for soft robotic finger-fluidic transistor systems corresponding to distinct  $\gamma$  designs: (Top)  $\gamma_1$ , (Middle)  $\gamma_2$ , and (Bottom)  $\gamma_3$ . Scale bars = 2 cm. (C–E) Experimental results for actuation force *versus*  $P_G$  for soft robotic fingers with embedded fluidic transistors with varying  $\gamma$  corresponding to  $P_G$  = (C) 2.5 kPa, (D) 5 kPa, and (E) 7.5 kPa. Error bands denote *S.D.*

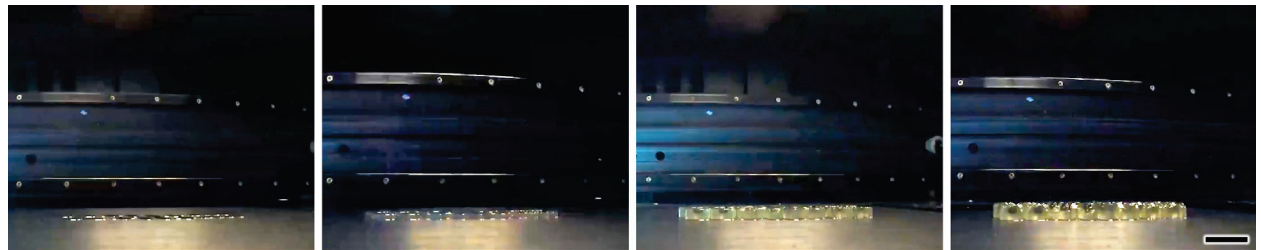


**Fig. S4.**

Sequential time-lapse images of the PolyJet 3D printing process for modular multi-material fluidic circuit elements. Scale bar = 10 cm.

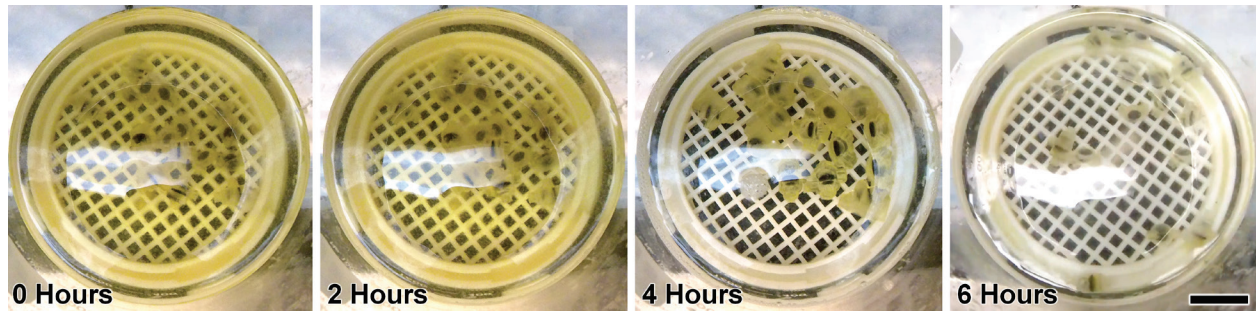


**Fig. S5.**

Sequential time-lapse images of entirely passive removal of the sacrificial support material, SUP706, from the external and internal regions of modular fluidic circuit elements following the PolyJet 3D printing process. The solution in which the components are submerged (with continuous magnetic stirring) comprises 2% NaOH and 2% Na<sub>2</sub>SiO<sub>3</sub> (*w/w*) in DI water. Solution replaced after 4 hours. Scale bar = 10 cm.

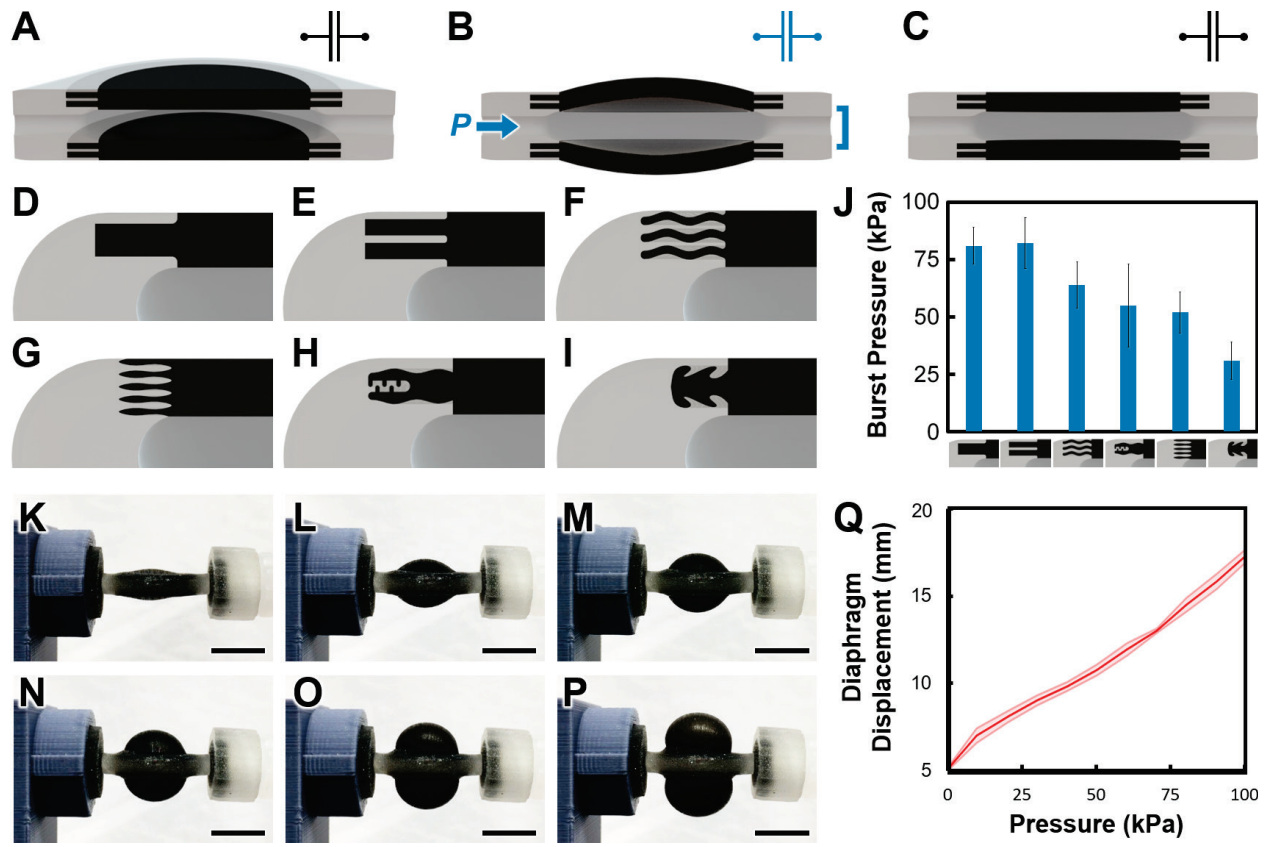


**Fig. S6.**

Multi-material PolyJet 3D printing-based fluidic capacitor. (A–C) Conceptual illustrations of the overall architecture (A) and input pressure ( $P$ )-based operating principles (B, C) for the fluidic capacitor, which comprises fully integrated rigid (white) and compliant (black) materials. (D–I) Distinct designs for the rigid-compliant material boundary interface. (J) Quantified results for burst-pressure experiments of the distinct rigid-compliant material boundary interfaces. Error bars denote *S.D.* (K–P) Experimental results for dual diaphragm inflation corresponding to  $P =$  (K) 0 kPa, (L) 20 kPa, (M) 40 kPa, (N) 60 kPa, (O) 80 kPa, and (P) 100 kPa. Scale bar = 1 cm. (Q) Quantified experimental results for diaphragm deformation *versus P*. Error bands denote *S.D.*

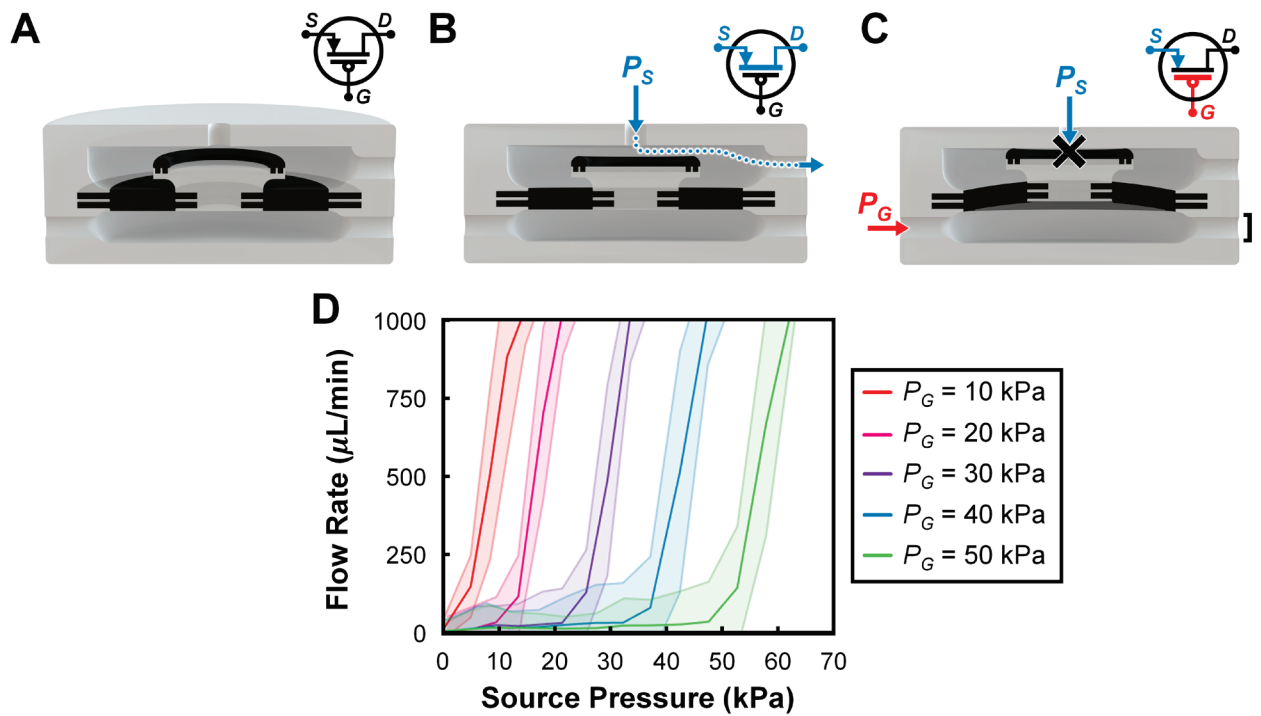


**Fig. S7.**

Multi-material PolyJet 3D printing-based alternative “normally open” fluidic transistor (without  $\gamma$  architecture). (A–C) Conceptual illustrations of the architecture (A) and  $P_G$ -based operating principles (B, C) for the fluidic transistor, which comprises fully integrated rigid (*white*) and compliant (*black*) materials. (D) Experimental results for source-to drain fluid flow ( $Q_{SD}$ ) *versus*  $P_S$  for varying  $P_G$  inputs. Error bands denote S.D.

## Supplementary Movie Captions

**Movie S1.** Time-lapse video of the PolyJet 3D printing process for single-print-run additive manufacturing of the multi-material constant flow-based soft robotic turtle comprising a fully integrated fluidic oscillator circuit. The materials printed include: (i) MED610 (a rigid material), (ii) Agilus30 (a compliant material), and (iii) SUP706 (a water-soluble sacrificial support material). Total print time  $\approx$  8 hr.

**Movie S2.** Theoretical COMSOL Multiphysics simulation results for diaphragm displacement under a fixed source pressure ( $P_s$ ) and increasing gate pressure ( $P_G$ ) for “normally open” fluidic transistors with differing pressure-gain ( $\gamma$ ) properties corresponding to diaphragm area ratios of: (left) 3.5 ( $\gamma_3$ ), (middle) 2 ( $\gamma_2$ ), and (right) 1 ( $\gamma_1$ ).

**Movie S3.** Experimental results for the constant flow-based soft robotic turtle comprising a fully integrated fluidic oscillator circuit under constant-flow conditions of 3 mL/min.

**Movie S4.** Theoretical and experimental results for deformation behavior of the biomimetic soft robotic finger and integration with a “normally open” fluidic transistor. (1) Simultaneous videos of (left) COMSOL Multiphysics simulation results and (right) digital image correlation (DIC)-processed experimental results both corresponding to pressure-induced fingertip deformation of 25 mm. (2) Video of a soft robotic finger with an embedded  $\gamma_3$  “normally open” fluidic transistor under varying  $P_s$  and  $P_G$  inputs (video speed = 2 $\times$ ). A kimwipe is placed adjacent to the drain output for qualitative visualization of exhaust flow associated with the various fluidic transistor states (based on the  $P_s$  and  $P_G$  inputs). Scale bars = 2 cm.

**Movie S5.** Time-lapse video of the PolyJet 3D printing process for single-print-run additive manufacturing of the preprogrammed, aperiodic fluidic input-based soft robotic “hand” with integrated fluidic circuitry. The printed materials include: (i) MED610 (a rigid material), (ii) Agilus30 (a compliant material), and (iii) SUP706 (a water-soluble sacrificial support material). Total print time  $\approx$  3.5 hr.

**Movie S6.** Experimental results for using the soft robotic “hand” with integrated fluidic circuitry to complete the first level of the “Super Mario Bros.” video game in real time in response to a pre-programmed  $P_G$  input ( $P_s$  programmed to remain constant). Pressure graph output (left) is tracked while the “Super Mario Bros” video game is played (middle) by the soft robotic hand interacting with a modified controller (right).

**Movie S7.** Support removal protocols for an integrated fluidic oscillator circuit. The key steps include: (0:00–0:15) removing the support material on the outside surface; (0:15–0:30) cleaning the female threaded connection; (0:30–0:45) clearing the internal fluidic channels with thin metal rods; (0:45–1:00) validating the clearance of the internal fluidic channels; and (1:00–1:21) connecting the fluidic circuit ports to peristaltic pumps and immersing it in a 2% NaOH and 2% Na<sub>2</sub>SiO<sub>3</sub> (w/w) in DI water with internal channels subjected to constant flow to dissolve any remaining support material. Total time for support removal protocols shown in video  $\approx$  25 min.